A Restoring Ability and Stability Analysis of Sailboats Across Different Points of Sail

Gyungju Kang
Department of Mechanical System Engineering, Kangwon National University, Samcheok, South Korea
gjk0222@naver.com (corresponding author)

Received: 13 November 2025 | Revised: 17 February 2026 | Accepted: 19 February 2026

Licensed under a CC-BY 4.0 license | Copyright (c) by the authors | *DOI: https://doi.org/10.48084/etasr.16253*

ABSTRACT

This study analyzes the restoring ability and stability of wind-powered leisure boats under varying angles of attack and side forces. Using fluid analysis and mathematical modeling, thrust and side forces were evaluated to clarify restoring characteristics. Results show that the angle of attack strongly affects sail aerodynamics, altering lift, drag, and corresponding thrust and side forces. Thrust and side force distributions identify optimal sailing angles, while restoring force analysis highlights the sail's dominant role in heeling moments over the hull. The angle of vanishing stability was 98°, confirming stable behavior even at large heel angles. The findings provide practical insights for improving the design and safety of wind-powered boats.

Keywords-restoring ability; heel moment; sailing boat; stability analysis; points of sail

I. INTRODUCTION

The growing leisure marine population has increased demand for low-cost, eco-friendly boats powered by renewable energy. Wind-powered leisure boats offer low operating costs but often face stability challenges that are directly related to wind-induced restoring forces. Previous studies have primarily focused on stability and roll reduction in powered vessels. Authors in [1, 2] reported that wind power and sail-angle control can reduce roll motion, while other authors in [3-8] investigated roll control through experimental, numerical, and passive damping approaches. However, limited research addressed wind-powered boats operating under side forces and varying angles of attack. The angle of attack alters lift, drag, and thrust, thereby influencing the stability of wind-powered boats. Recent CFD-based studies have further refined the understanding of sailboat stability mechanisms. Authors in [9] investigated the aerodynamic performance of wingsails numerically and showed that increasing the heel angle decreases thrust and lift while increasing drag. Authors in [10] analyzed the coupled forces between the sail and the hull and demonstrated that separating aerodynamic and hydrodynamic loads is essential for accurate stability prediction. Building on these findings, the present study aims to clarify the relationship between the aerodynamic and hydrodynamic forces acting on a small wind-powered boat and their effect on the restoring ability and overall stability.

Recent studies [11,12] incorporated reinforcement-learning-based navigation and control for wind- or rotor-assisted marine vehicles, highlighting the growing importance of intelligent and coupled aerodynamic–hydrodynamic approaches. This trend provides complementary context to the present stability-focused investigation. Unlike prior roll-control- or aero-only studies, this work integrates aerodynamic and hydrodynamic analyses with point-of-sail restoring-moment diagrams in a CFD-based framework to provide a quantitative stability assessment for small wind-powered leisure boats.

II. THEORETICAL BACKGROUND

The analysis defines geometry, performs CFD over attack and heel angles, decomposes forces, and evaluates restoring moments for stability. The flow follows the incompressible continuity and Navier–Stokes equations:

$$\nabla \cdot \mathrm{u} = 0 \tag{1}$$

In tensor form, the Navier–Stokes equation is:

$$\left(\frac{\partial}{\partial t} + u_j \frac{\partial}{\partial x_j} - \nu \frac{\partial^2}{\partial x_j \partial x_j}\right) u_i = -\frac{\partial w}{\partial x_i} + g_i \tag{2}$$

where u is the flow velocity, and g is the body acceleration acting on the continuum.

Figure 1 shows the variable correlation for thrust and side-force evaluation. α is the angle of attack, θ the sail angle, and V the wind direction; L, D, T and $S.F$ denote lift, drag, thrust, and side force. A local $x-y$ coordinate system normal and tangential to the sail defines the load components F_x and F_y, from which lift and drag are derived as follows:

$$\begin{Bmatrix} L \\ D \end{Bmatrix} = \begin{bmatrix} \cos\alpha & -\sin\alpha \\ \sin\alpha & \cos\alpha \end{bmatrix} \begin{Bmatrix} F_x \\ F_y \end{Bmatrix} \tag{3}$$

Thrust and side force in terms of F_x and F_y are expressed by:

$$\begin{Bmatrix} T \\ S.\mathrm{F} \end{Bmatrix} = \begin{bmatrix} \sin\theta & -\cos\theta \\ \cos\theta & \sin\theta \end{bmatrix} \begin{Bmatrix} F_x \\ F_y \end{Bmatrix} \tag{4}$$

From (3)–(4), thrust and side force in terms of lift and drag are expressed by:

$$\begin{Bmatrix} T \\ S.F \end{Bmatrix} = \begin{bmatrix} \sin(\alpha+\theta) & -\cos(\alpha+\theta) \\ \cos(\alpha+\theta) & \sin(\alpha+\theta) \end{bmatrix} \begin{Bmatrix} L \\ D \end{Bmatrix} \quad (5)$$

Thrust and side force are analyzed as functions of the angle of attack (α) and sail angle (θ). Figure 2 shows the points of sail relative to the wind.

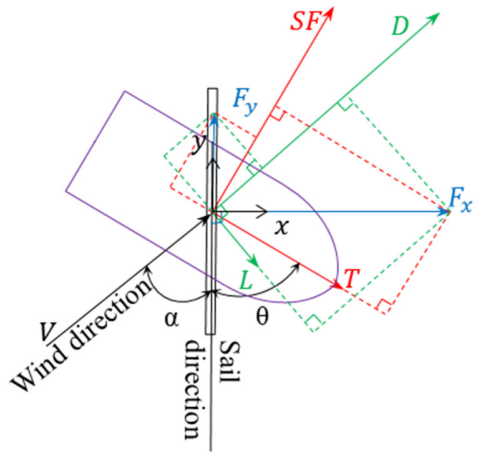

Fig. 1. Ship body-fixed coordinate system.

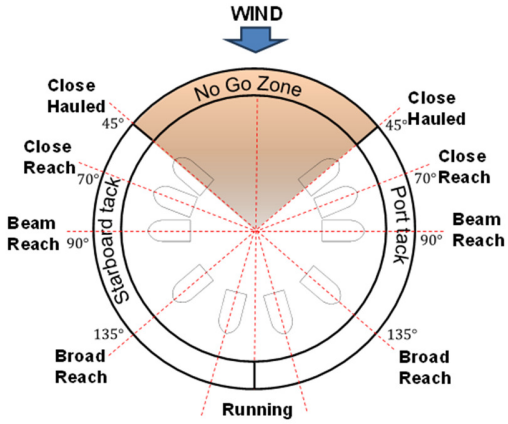

Fig. 2. Points of sail.

The points of sail include close-hauled, close reach, beam reach, broad reach, and running, while the no-go zone denotes a non-navigable direction [13]. This study examines the thrust and side force for these sailing conditions. For close-hauled, beam reach, and broad reach, the angles between thrust and wind are approximately 45°, 90°, and 135°, respectively [14].

The exact restoring ability is difficult to calculate due to variations in sail shape and rigging; therefore, the following assumptions are adopted:

1. The sail is flat and the wind blows constantly.
2. The Center of Effect (CE) is at the centroid of the sail.
3. The Center of Lateral Resistance (CLR) is at the centroid of the underwater central longitudinal section.

Let h be the distance between CE and CLR and M_w the heeling moment. The side force is expressed as:

$$M_w = S.F \cdot h \quad (6)$$

In addition, the restoring moment $M_\emptyset$ can be expressed as:

$$M_\emptyset = \Delta \cdot GM \cdot \sin\phi \quad (7)$$

Combining (6) and (7) yields:

$$S.F \cdot h = \Delta \cdot GM \cdot \sin\phi \quad (8a)$$

$$\sin\phi = \frac{S.F \cdot h}{\Delta \cdot GM} \quad (8b)$$

From (6), the heel moment is proportional to the side force and h, and inversely proportional to Δ and GM. From Figure 3, at inclination ϕ, M_w and M_ϕ are:

$$M_w = S.F \cdot \cos\phi \cdot h\cos\phi = S.F \cdot h\cos^2\phi \quad (9)$$

$$M_\emptyset = \Delta \cdot GM \cdot \sin\phi \quad (10)$$

Equation (10) applies for inclination ϕ <10° [15]; for ϕ > 10°, the metacenter shifts (Figure 4), and M_ϕ is:

$$M_\emptyset = \Delta \cdot GZ = \Delta\left(\frac{v \cdot h_e h_i}{\nabla} - B_0 G\sin\phi\right) \quad (11a)$$

$$= \Delta\left(\frac{v \cdot h_e h_i}{\nabla}\right) - \Delta \cdot B_0 G\sin\phi \quad (11b)$$

where v is the submerged boat volume at a given inclination. In (11b), $\Delta(v \cdot h_e h_i)/\nabla$ represents the shape-related restoring force, while $\Delta \cdot B_0 G\sin\phi$ denotes the weight-related restoration due to the center of gravity. The restoring moment is obtained by subtracting the weight restoration from the shape restoring force.

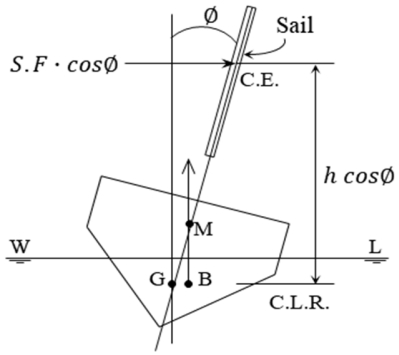

Fig. 3. Side force and heel of the boat with the sail

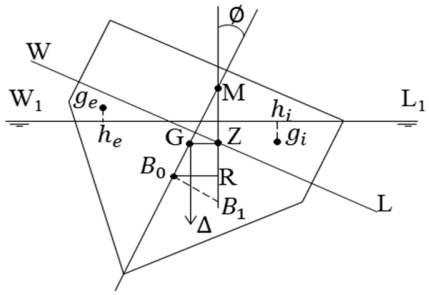

Fig. 4. Schematic of the boat with a heel of >10°.

III. FEM FLUID ANALYSIS

A. Analysis Model

A small leisure boat model using a 0.6 × 1.25 m sail was analyzed (Table I). The geometry is shown in Figure 5.

TABLE I. PRINCIPAL DIMENSIONS OF THE BOAT

Length	L.O.A.	1.6 m
Length	L.B.P.	1.5 m
Breadth	B	0.7 m
Depth	D	0.5 m
Design Draft	D	0.25

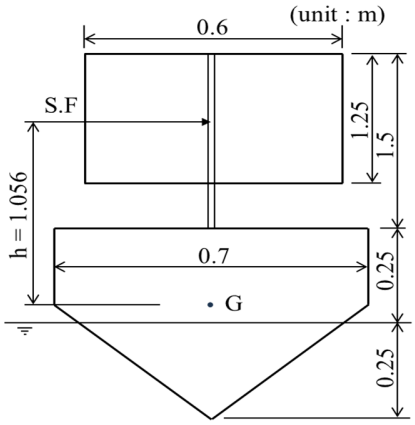

Fig. 5. Dimensions of the hull and sail of the model.

B. Grid Generation

A refined triangular-prism mesh (~670k cells) was generated in ANSYS CFX-Mesh.

C. Aerodynamic Analysis of the Sail

Total forces were decomposed into aerodynamic and hydrodynamic components. Aerodynamic forces were obtained by pressure integration on the sail, while hydrodynamic forces acted on the submerged hull. Their combination yielded thrust, side force, and heeling moment governing stability. Simulations used a uniform inlet wind speed of 5 m/s (Beaufort 3) [16, 17] over attack angles of 5°–90° at 5° intervals, with atmospheric outlet pressure and no-slip sail boundaries. Figures 6 and 7 show the computational domain and resulting vertical wing-tip vortices, which agree with experimental and numerical observations [18, 19].

D. Aerodynamic Analysis Results

Figure 8 shows F_x(normal) and F_y(tangential), with $F_x > F_y$. Lift and drag derived from (3) increase and peak at ~30°, whereas thrust and side force follow (3)–(4). The apparent wind angle is:

$$\beta = \alpha + \theta \tag{12}$$

Figure 11 shows the aerodynamic variation with α and θ.

Equation (13) shows drag and lift as cubic polynomials of the angle of attack:

$$\begin{Bmatrix} D \\ L \end{Bmatrix} = \begin{bmatrix} -0.000025 & 0.002511 & 0.136597 & -0.151552 \\ 0.000048 & -0.010535 & 0.556213 & 0.719314 \end{bmatrix} \begin{Bmatrix} \alpha^3 \\ \alpha^2 \\ \alpha \\ 1 \end{Bmatrix} \tag{13}$$

Coefficients in (13) were fitted in Matlab®; lift and drag coefficients follow (14a)–(14b):

$$C_L = \frac{L}{\frac{1}{2}\rho V^2 \cdot A_S} \tag{14a}$$

$$C_D = \frac{D}{\frac{1}{2}\rho V^2 \cdot A_S} \tag{14b}$$

Figure 9 shows the drag polar, where the lift coefficient C_L increases up to about 30° and then decreases, while the drag coefficient C_D rises continuously with the angle of attack. Thrust is expressed by (15), and its distribution with respect to angle of attack and θ is shown in Figure 10.

$$\text{Thrust} = \sin(\alpha + \theta)\, L - \cos(\alpha + \theta)\, D \tag{15}$$

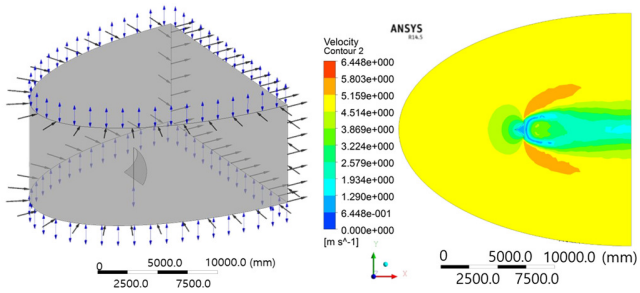

Fig. 6. Computational domain and boundary conditions.

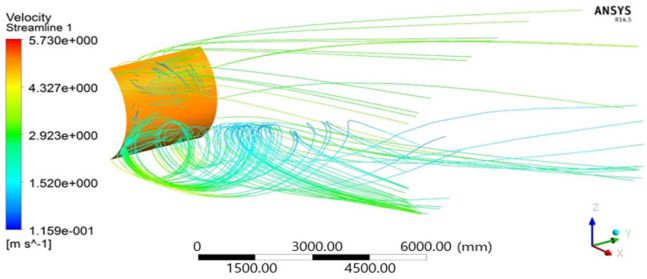

Fig. 7. Velocity field and streamlines of the rectangular sail.

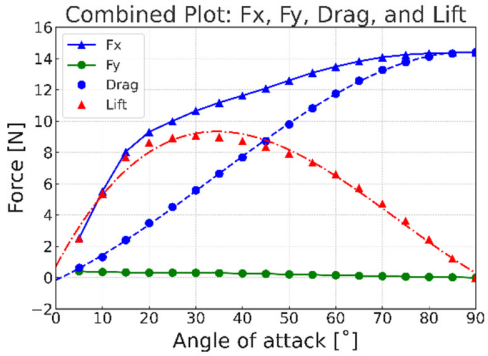

Fig. 8. Variation of *Fx*, *Fy*, Drag, and Lift vs. angle of attack.

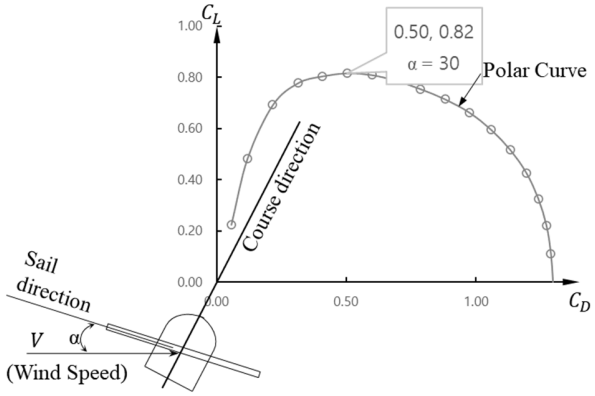

Fig. 9. Drag polar using C_L and C_D with respect to the angle of attack.

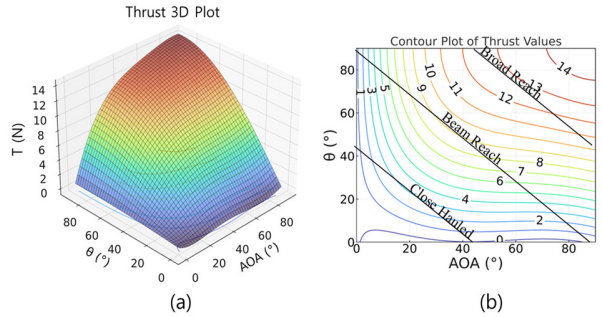

Fig. 10. Thrust distributions and contour plot: (a) Thrust distribution, (b) thrust distribution and point of sail diagram.

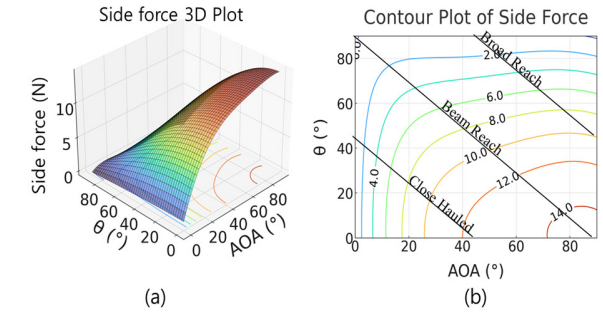

Fig. 11. Side force distribution and contour plot: (a) Side force distribution, (b) side force distribution and point of sail diagram.

In Figure 10(a), we observe the variation of the angle of attack (α) ranging from 0° to 90°. Here, the sail angle (θ), resulting in the apparent wind angle (β). Equation (12) represents this relationship. Figure 10(a) displays the thrust in all directions as influenced by the direction of travel and the angle of attack. Figure 10(b) presents the 3D thrust contour, integrated with point-of-sail lines (close hauled, beam reach, broad reach). This diagram enables quick identification of the angle of attack that produces maximum thrust for each sailing direction. For beam reach, the optimum α is approximately 65°. Figure 11(a) shows the 3D side-force distribution, and Figure 11(b) its contour representation integrated with point-of-sail lines. For beam reach, the maximum lateral force occurs at $\alpha \approx$ 90°, consistent with the expectation that wind from the side produces the highest load. The side force is given by (16) and is plotted in Figure 11.

$$\text{Side Force} = \cos(\alpha + \theta)\, L + \sin(\alpha + \theta)\, D \qquad (16)$$

IV. STABILITY ANALYSIS OF SAILBOATS IN VARIOUS SAILING CONDITIONS

A. *Stability Characteristics and Heel Moment Analysis*

The sailboat's stability was examined under three points of sail: close hauled, beam reach, and broad reach (Figure 12). The heeling moment distribution for heel angles from 0° to 90° shows that the moment generated by the sail is much greater than that without it, indicating that only the sail's effect needs to be considered. For close hauled, the maximum heeling moment occurs at α ≈ 60°, where the sail aligns closely with the sailing direction. For beam reach and broad reach, the peak occurs at α ≈ 90°, as the wind blows directly from the side, producing the largest lateral load. Overall, the heeling moment is governed primarily by the sail rather than the hull, confirming that hull-side effects have negligible influence on heel-moment magnitude.

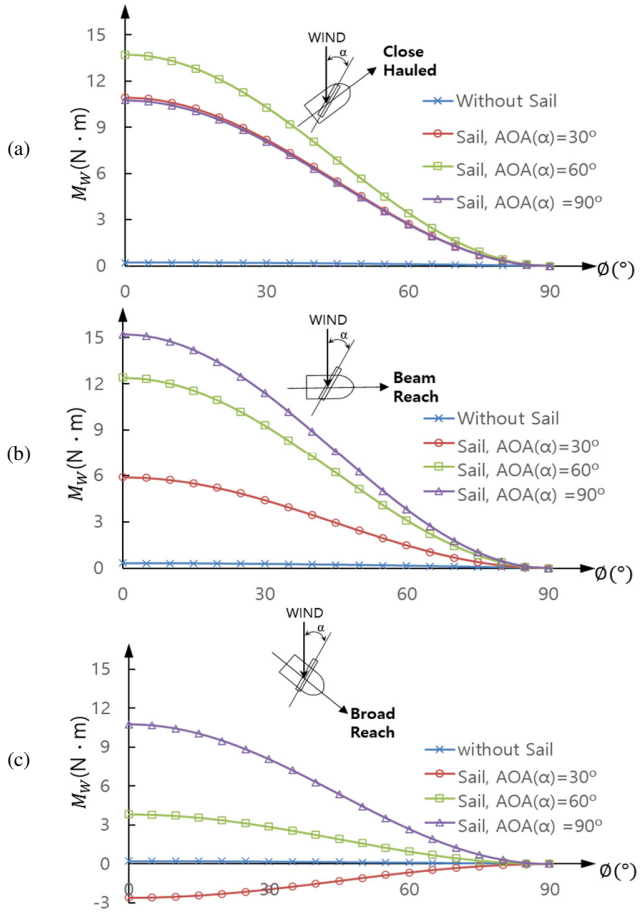

Fig. 12. Heel moment with respect to heel angle: (a) Close hauled, (b) beam reach, (c) broad reach.

B. Side Force Variations and Stability Analysis

Figure 13 presents the variation of side force with respect to α at apparent wind angle β. At β = 90°, the relationship between side force and α shows a consistent trend: as α increases, the side force also increases and reaches a maximum at α = 90°, indicating stronger aerodynamic influence at higher β. This study investigates side-force distributions at β = 45°, 90°, and 135°. The roll angle φ_0, where wind-induced work equals the restoring force under constant wind, remains 10° or lower for all orientations, implying stable behavior with a maximum inclination below 10°, even during a 90° turn.

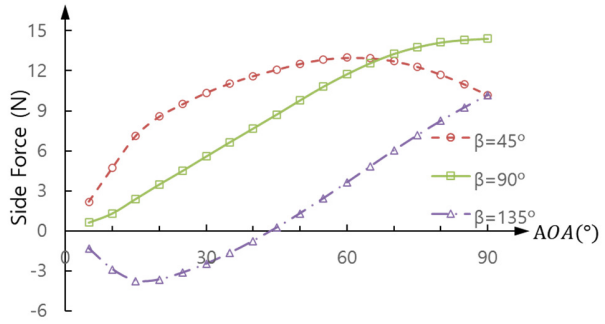

Fig. 13. Variations in side force with respect to α.

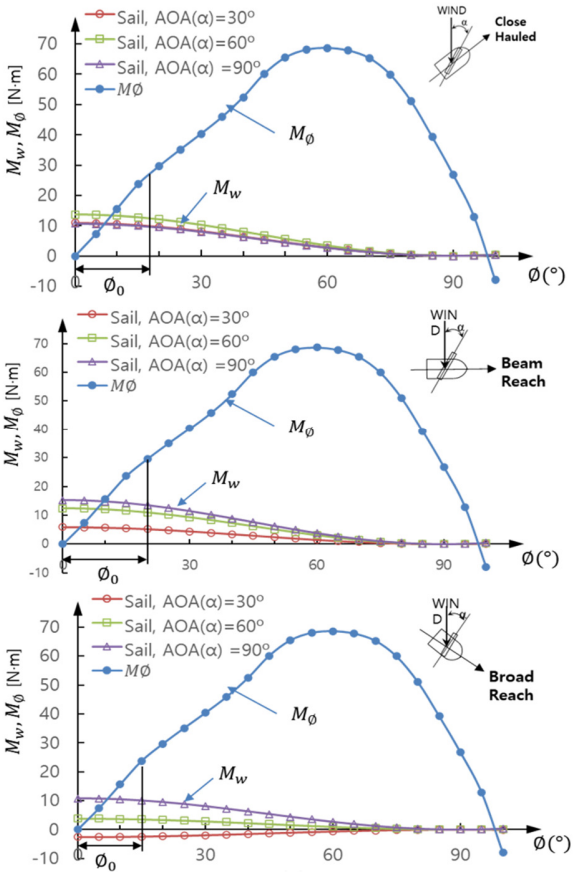

Fig. 14. Distribution of heel moment M_w and restoring moment $M_\emptyset$ for heel angle at β = 45°, 90°, and 135°: (a) Close hauled; (b) beam reach; (c) broad reach.

Figure 14 illustrates the distribution of the heeling moment M_w and restoring moment M_ϕ with heel inclination for β = 45°, 90°, and 135°. The heeling moment represents wind energy, whereas the righting moment represents restoring energy. The roll angle φ_0 denotes the inclination at which these energies are in equilibrium under steady wind conditions [16]; consequently, the boat assumes a tipped angle φ_0.

Table II displays the φ_0 values for each α in different sailing directions. The optimal value of 19° occurs at α = 90° during beam reach, producing the highest lateral tilt and representing the maximum inclination angle. Accordingly, 19° can be considered a safe stability setting for beam reach maneuvers.

TABLE II. EVALUATION OF Φ_0 VALUES FOR DIFFERENT ANGLES OF ATTACK AND SAILBOAT DIRECTIONS

Direction	α [°]		
	30	60	90
Close hauled	14	18	14
Beam reach	7	16	19
Broad reach	-	6	13

C. Evaluation of the Restoring Force of the Leisure Boat

Figure 15 shows the trajectory of the center of buoyancy with heel slope, exhibiting regular fluctuations that indicate favorable stability. Figure 16 presents the GZ curve (S.S.C.) versus heel angle, where the angle of vanishing stability $\phi_r$is 98°, and a restoring force is maintained even at 90° inclination. At ϕ = 0°, the curve starts at 57.3 (1 rad) with a metacentric height GM = 0.076 m. This GM value defines the initial restoring force, while the GZ curve is used for restoring-force calculations beyond 10° inclination.

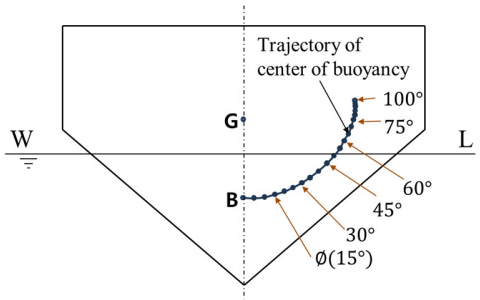

Fig. 15. Trajectory of center of boyancy with respect to heel slope.

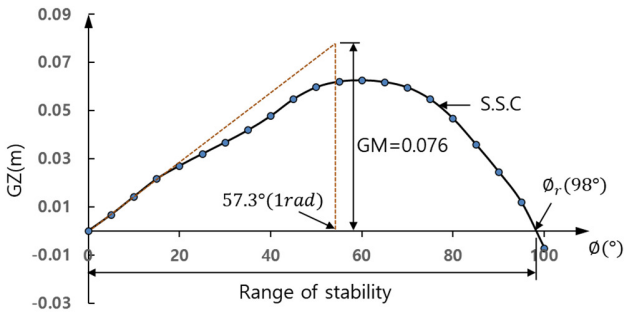

Fig. 16. Static restoring curve of the leisure boat.

V. CONCLUSIONS

This study investigated the restoring ability and stability of a single wind-powered leisure boat configuration operating under various angles of attack and side forces. This integrated aerodynamic–hydrodynamic evaluation framework distinguishes the present work from prior roll-control-oriented or purely aerodynamic studies. Mathematical formulations for thrust and side force were developed through CFD analysis to quantitatively evaluate the restoring performance. The results demonstrated that the angle of attack (α) strongly affects aerodynamic characteristics around the sail. Variations in α alter lift and drag, which in turn modify thrust and side force generation. The thrust and side force distribution diagrams help identify the angles of attack that yield maximum performance for specific sailing directions.

The restoring force analysis revealed that the sail predominantly governs the heeling moment, while the hull's influence remains limited under side loading. The angle of vanishing stability was found to be approximately 98°, confirming that the vessel maintains stability even during a 90° turn.

These findings provide practical guidance for optimizing the sail–hull aerodynamic balance in small leisure boats to enhance stability and control under varying wind conditions. Although this work focuses on a single boat configuration, the presented approach can serve as a methodological reference for future studies on the stability of wind-powered vessels.

Future work will include experimental validation and extended simulations under various hull configurations and environmental conditions.

REFERENCES

[1] Y. Yoshimura, Y. Igarashi, T. Kuroda, and M. Kikumoto, "Roll-damping Control by Sail-angle," *Journal of the Japan Society of Naval Architects and Ocean Engineers*, vol. 2, pp. 237–242, Jan. 2005, https://doi.org/10.2534/jjasnaoe.2.237.

[2] Y. Tahara, Y. Masuyama, T. Fukasawa, and M. Katori, "Sail Performance Analysis of Sailing Yachts by Numerical Calculations and Experiments," in *Fluid Dynamics, Computational Modeling and Applications*, IntechOpen, https://doi.org/10.5772/28440, 2012.

[3] G. H. Chae and Y. B. Kim, "An experimental study on the rolling motion control of a ship based on LMI approach," *Journal of the Korea Society of Ocean Engineers*, vol. 17, no. 2, pp. 60–66, Apr. 2003.

[4] U. C. Jeong, S. H. Jeong, and H. W. Chun, "A study on the hull form development and resistance performance of a high-speed coastal patrol boat," *Journal of Ocean Engineering and Technology*, vol. 18, no. 3, pp. 44–49, Jul. 2004.

[5] Y. B. Kim, K. S. Lee, J. H. Kim, and G. H. Chae, "A study on development of an anti-rolling system for ship stability improvement," *Journal of the Korean Society of Marine Environment and Safety*, vol. 11, no. 1, pp. 23–28, Feb. 2005.

[6] S.-K. Lee, J.-M. You, H.-h. Lee, and S.-H. Rhee, "Experimental Study on Free Roll Decay Motions of a Damaged Ship for CFD Validation Database," *Journal of the Society of Naval Architects of Korea*, vol. 49, no. 1, Feb. 2012, https://doi.org/10.3744/SNAK.2012.49.1.52.

[7] K. S. Youssef, S. A. Ragab, A. H. Nayfeh, and D. T. Mook, "Design of passive anti-roll tanks for roll stabilization in the nonlinear range," *Ocean Engineering*, vol. 29, no. 2, pp. 177–192, Feb. 2002, https://doi.org/10.1016/S0029-8018(01)00021-X.

[8] O. A. Marzouk and A. H. Nayfeh, "Control of ship roll using passive and active anti-roll tanks," *Ocean Engineering*, vol. 36, no. 9, pp. 661–671, Jul. 2009, https://doi.org/10.1016/j.oceaneng.2009.03.005.

[9] R. Zhang *et al.*, "Numerical investigation on the effects of heel on the aerodynamic performance of wing sails," *Ocean Engineering*, vol. 305, Aug. 2024, Art. no. 117897, https://doi.org/10.1016/j.oceaneng.2024.117897.

[10] S. Liu, Z. Yu, T. Wang, Y. Chen, Y. Zhang, and Y. Cai, "MPC-based collaborative control of sail and rudder for unmanned sailboat," *Journal of Marine Science and Engineering*, vol. 11, no. 2, Feb. 2023, Art. no. 460, https://doi.org/10.3390/jmse11020460.

[11] G. Zhang, Z. Li, J. Li, Y. Shu, and X. Zhang, "Reinforcement learning-driven autonomous navigation strategy for rotor-assisted vehicles via integral event-triggered mechanism," *Transportation Research Part D: Transport and Environment*, vol. 146, Sep. 2025, Art. no. 104841, https://doi.org/10.1016/j.trd.2025.104841.

[12] Z. Li, G. Zhang, and P. Liu, "Event-triggered optimal path-following control for wind-assisted autonomous surface vehicles via actor–critic reinforcement learning," *Journal of Marine Science and Engineering*, vol. 13, no. 11, 2025, Art. no. 2117, https://doi.org/10.3390/jmse13112117.

[13] "The 5 points of sail: discover the sailboat's angles to the wind," *Sailing Ellidah*, [Online]. Available: https://sailingellidah.com/points-of-sail.

[14] W. Porter, "Points of Sail Explained (with Degrees and Diagram)," *ImproveSailing*. https://improvesailing.com/sailing/trimming/points-of-sail.

[15] D. Y. Jeong, *Ship Design*, Seoul, Korea: Myungjin Books, 2012.

[16] S. K. Lee, *Ship Calculation and Stability*, Seoul, Korea: GS Intervision, 2012.

[17] *Manual on Codes – Part A*, WMO-No. 306, Section E. I.1, Geneva, Switzerland: World Meteorological Organization (WMO), 2019.

[18] A. Arredondo-Galeana and I. M. Viola, "The leading-edge vortex of yacht sails," *Ocean Engineering*, vol. 159, pp. 552–562, Feb. 2018, https://doi.org/10.1016/j.oceaneng.2018.02.029.

[19] A. Arredondo-Galeana, H. Babinsky, and I. M. Viola, "Vortex flow of downwind sails," *Flow*, vol. 3, Jan. 2023, Art. no. E8, https://doi.org/10.1017/flo.2023.1.